applied sciences

MDPI

Article

Investigation on Seakeeping of WTIVs Considering the Effect of Leg-Spudcan Well

Mingsheng Xiahou [1,2,*], Yuefeng Wei [2], Jinjia Wu [2], Xueqin Liu [2], Wei Lu [2] and Deqing Yang [1]

[1] State Key Laboratory of Ocean Engineering, School of Ocean Engineering, Shanghai Jiao Tong University, Shanghai 200240, China; yangdq@sjtu.edu.cn
[2] Marine Design & Research Institute of China, Shanghai 200011, China; yfwei2015@163.com (Y.W.); jinjia_wu@163.com (J.W.); liuxq02@163.com (X.L.); 15542387923@163.com (W.L.)
* Correspondence: xhmsjd@126.com

Abstract

Aiming at the limited applicability of traditional empirical formulas in roll prediction for offshore wind turbine installation vessels (WTIVs), this study proposes a collaborative verification method that integrates model tests with Computational Fluid Dynamics (CFD) simulations. This approach reveals the influence mechanism of the fluid trapped in the leg-spudcan well region on the roll period and damping, facilitating high-precision prediction. A numerical model of the WTIV in a jack-up operating condition was established, and a CFD method based on the RANS equations was employed alongside experimental data for synergistic analysis. The results demonstrate that the fluid in the leg-spudcan well generates a significant additional moment of inertia, which reduces the natural roll period by approximately 7% and increases the damping coefficient by approximately 58%. Furthermore, an increase in leg length leads to a linear increase in damping and a linear decrease in the roll period. The motion response transfer functions derived from tests and the motion response errors of key structures in irregular waves are generally less than 10%. On this basis, a motion response conversion method applicable to any location on the entire ship is derived, providing a reliable numerical analysis tool for WTIV seakeeping evaluation and operational window assessment.

Keywords: free roll decay; irregular waves; anti-roll tank; leg-spudcan well

check for updates

Academic Editor: Atsushi Mase

Received: 23 October 2025
Revised: 27 November 2025
Accepted: 28 November 2025
Published: 30 November 2025

Citation: Xiahou, M.; Wei, Y.; Wu, J.; Liu, X.; Lu, W.; Yang, D. Investigation on Seakeeping of WTIVs Considering the Effect of Leg-Spudcan Well. *Appl. Sci.* **2025**, *15*, 12701. https://doi.org/10.3390/app152312701

Copyright: © 2025 by the authors. Licensee MDPI, Basel, Switzerland. This article is an open access article distributed under the terms and conditions of the Creative Commons Attribution (CC BY) license (https://creativecommons.org/licenses/by/4.0/).

1. Introduction

With the acceleration of the global energy structure to low-carbon transformation, the offshore wind power industry is developing towards deep-sea environments and larger-capacity turbine units, which puts forward higher requirements for the operation performance of Wind Turbine Installation Vessel. The leg-spudcan serves as a core component of this ship type. During operations, the spudcans are lowered to the seabed, and the hull is raised above the water surface via the support of the legs, forming a working platform that is less affected by wave and current loads. During transit, the legs are fully retracted into the spudcan wells (which are void structures vertically penetrating the hull and connecting the deck to the bottom) to minimize the ship's navigation resistance [1]. The new generation of integrated WTIVs features a maximum operating depth of over 70 m, leg lengths exceeding 120 m, main crane hook heights (above the waterline) greater than 160 m, and maximum lifting capacities surpassing 1500 tons, enabling the installation of large offshore wind turbines rated at 16 MW and above. However, the high-elevation

legs, heavy lifting equipment, and multi-layer stacked wind turbine components (such as ultra-hundred-meter blades and large towers) result in a significantly higher center of gravity and larger wind area compared to conventional transport ships. This substantially amplifies the six-degree-of-freedom motion responses (particularly roll, heave, and pitch) during transit and dynamic positioning (DP) jack-up operations [2]. Consequently, the dynamic inertial loads on key structures such as the legs, jacking cases, helideck, and crane boom rests are increased. The impact at the spudcan–seabed interface is also significantly heightened [3], which can even lead to fatigue damage in the leg structure during long-distance navigation. Notably, heave motion directly shortens the operational weather window, and the probability of operation interruption under critical conditions can increase by more than 60% [4]. Therefore, seakeeping prediction for WTIVs must move beyond the traditional ship analysis framework and establish an evaluation system that couples motion response with structural strength. This is essential for optimizing the sea state threshold for safe operation and thereby improving operational efficiency.

Meanwhile, model testing and numerical prediction are two core methodologies in ship seakeeping research. Among these, traditional potential flow theory offers high computational efficiency for predicting motion responses in the frequency or time domain. Based on three-dimensional potential flow theory, Xu Chao et al. [5,6] conducted numerical simulations of the frequency and time domain motion responses of a wind turbine installation vessel. They verified the accuracy of their predictions for sailing resistance, Response Amplitude Operators (RAOs), and motion amplitude in irregular waves through model tests, revealing the operational risk that ship motion amplitude may exceed limits under a ten-year sea state in the North Atlantic. Similarly, Zhang et al. [7] employed SESAM software based on three-dimensional nonlinear time-domain potential flow theory to analyze and verify the reliability of a simulation method for the motion response of a KCS container ship in regular waves. They compared and analyzed the ship's roll motion response under different initial roll angles, speeds, wavelengths, and wave steepness. Jiao et al. [8] conducted a large-scale model field test in the sea area of Huludao, China, obtaining short-term response time histories of ship motion and slamming loads in real short-crested waves, which revealed the nonlinear characteristics of both. Guo Jing et al. [9] performed seakeeping tests on a ship under coastal wind and wave conditions using a remote telemetry large-scale self-propelled model, verifying the nonlinear characteristics of the ship's heave motion. However, such physical tests are often expensive and limited in their coverage of conditions, making it difficult to meet the multi-condition and multi-scale refined design requirements of WTIVs.

In recent years, with the improvement of computing power, CFD technology has provided a powerful new tool for ship seakeeping research, enabling more accurate simulation of viscous effects and nonlinear phenomena. Song et al. [10] used STAR-CCM+ to simulate the pitch and heave motion responses of an operation and maintenance mother ship in regular waves, verifying the reliability of the CFD method based on the RANS equations for viscous flow analysis. Another study by Song et al. [11] revealed the asymmetric characteristics of hull motion in short-crested waves through two-way cross-wave simulation. Addressing the key issue of roll damping, Li et al. [12] optimized the bilge keel design of an ocean fishing vessel using CFD, demonstrating an improvement in roll damping of more than 20%, which provides a reference for bilge keel optimization on WTIVs. Feng [13] demonstrated the significant influence of hull configuration on roll damping through a CFD study of a catamaran. Irkal et al. [14] simulated the free decay motion of a two-dimensional hull section (including different bilge keel configurations) using CFD. Combined with experimental verification, they found high consistency between the CFD and experimental results, noting that the presence of a bilge keel introduces nonlinearity to

the roll damping, which increases with bilge keel size. The research of Kianejad et al. [15], Devolder et al. [16], and Ghamari et al. [17] further verified the effectiveness and reliability of CFD for forced roll simulation, forced roll analysis, and ship roll damping calculation, respectively. Byrdal et al. [18] used the RANS equations combined with the SST turbulence model to systematically analyze the influence of the vertical position of the WTIV's center of gravity and bilge keel installation on roll damping under different load conditions, based on a series of model test results. They also compared the prediction results for extreme roll motion in irregular waves with traditional empirical methods. Gao et al. (2019) [19] and Ding et al. (2022) [20] investigated wave resonance phenomena in the narrow gap between two fixed marine structures. They conducted high-fidelity numerical simulations using CFD, which accounts for fluid viscous effects and nonlinearities, to capture vortex shedding and its dissipation. Lei et al. (2023) [21] proposed a CFD-assisted frequency-domain method for predicting the motion and structural loads of floating structures with damping plates. This approach involves calculating nonlinear damping coefficients through CFD simulations, which are subsequently applied in a linearized frequency-domain analysis.

Despite significant progress having been made in research, several challenges and gaps remain specific to WTIVs. Traditional potential flow theory ignores viscous effects, often leading to an underestimation of damping. Although CFD can capture the contributions of vortex shedding and bilge keels, the influence mechanism of the additional moment of inertia—generated by liquid sloshing in the leg-spudcan well region—on the roll period and damping remains unclear. In particular, research on high-precision prediction methods for damping and period for such special ship types is still in its infancy. Furthermore, existing model tests and multi-body dynamics analyses mostly focus on the overall motion of the hull, with insufficient quantitative analysis of the inertial acceleration of key parts such as the legs, jacking cases, and helideck in waves.

To address these limitations, this study constructs a comprehensive analysis framework that combines ship model tests with CFD-based three-dimensional (3D) numerical towing tank simulations to systematically evaluate the seakeeping performance of the new generation of WTIVs. Through free roll decay tests in calm water and numerical simulations of the viscous flow field, the roll damping coefficient and natural period under different leg deployment conditions are quantified. Simultaneously, by employing the response amplitude operator (RAO) of the six-degree-of-freedom motion response, the extreme motion responses at key positions of the hull in irregular waves are predicted. The core innovation of this study lies in identifying and quantifying the "free-flooding anti-roll tank" effect created by the fluid in the confined well area when the legs are fully retracted, and in systematically clarifying its suppression mechanism on roll motion. On this basis, calculation methods for inertial loads in different regions of the hull under irregular waves and for the impact loads on legs during dynamic positioning (DP) jack-up operations are proposed. This work provides an important theoretical reference and a practical analysis tool for the strength design of key structures (such as legs, spudcans, crane boom rests, and helidecks) and for the overall seakeeping assessment of the vessel.

2. Seakeeping Test Methods for the WTIV

2.1. Coordinate System and Wave Direction Definition

The definition of the coordinate system used in this study is shown in Figure 1. Wave directions follow nautical convention, with the port side defined as positive and the starboard side as negative. The specific definitions are as follows:

- Head Wave: Angle between wave direction and ship heading is between $\pm 165^{\circ}$ and $\pm 180^{\circ}$.

- ➢ Following Wave: Angle between wave direction and ship heading is between ±0° and ±15°.
- ➢ Beam Wave: Angle between wave direction and ship heading is between ±75° and ±105°.
- ➢ Bow Quartering Wave: Angle between wave direction and ship heading is between ±105° and ±165°.
- ➢ Stern Quartering Wave: Angle between wave direction and ship heading is between ±15° and ±75°.

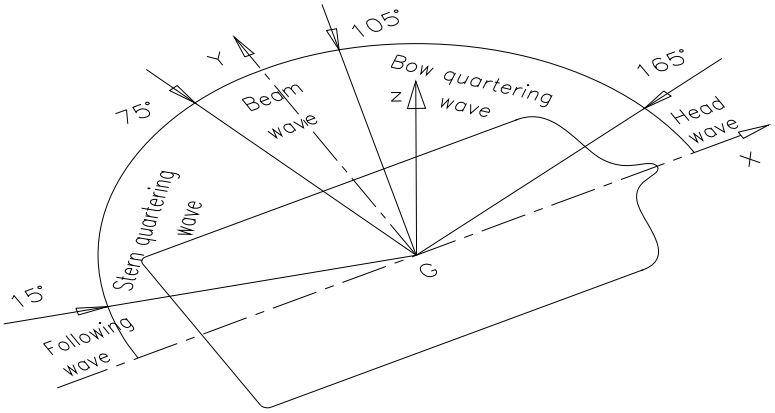


Figure 1. Coordinate System and Wave Direction Definition.

The experiment was carried out in a large towing tank with a scale of 280 m (length) × 10 m (width) × 5 m (water depth), which has the ability to simulate a variety of typical ocean wave environments. According to the similarity theory, the similarity criteria of the Froude number (*Fr*) and Strouhal number (*St*) are used to ensure the dynamic similarity between the model and the full-scale vessel. Considering the main scale parameters of WTIV (see Table 1), the characteristics of working environment and the conditions of test facilities, the geometric scale ratio is determined to be λ = 1:35. This scale ensures test economy while accurately reflecting the full-scale vessel's hydrodynamic characteristics.

Table 1. Ship particulars represented by ship model.

Items	Full Scale	Test Model
Length overall L_{oa}, m	126	3.6
Length on water line L_{wl}, m	125	3.5714
Breadth B, m	50	1.4286
Depth D, m	10	0.2857
Design draught d, m	6.2	0.1771
Block coefficient C_B	0.8	0.8
Displacement △, t	32,530	0.7403
Center of Gravity *LCG*, m	62.5	1.7857
Center of Gravity *VCG*, m	20.1	0.5743
Roll gyration radius R_{xx}, m	26.87	0.7677
Pitch gyration radius R_{yy}, m	43.84	1.2526
Yaw gyration radius R_{zz}, m	40.25	1.15

2.2. Test Content and Procedure

The model tests primarily included the following three parts:

(1) Free Roll Decay Tests in Calm Water

When the ship deviates from the roll equilibrium position in still water, it will gradually return to the initial equilibrium state under the action of the hydrostatic restoring moment. The free roll decay test involves collecting the time history of the model's free roll decay motion in calm water and analyzing its decay curve to obtain the natural roll period and non-dimensional damping coefficient. The dimensionless damping coefficient is calculated according to the following Formula [22]:

$$\mu = \frac{1}{\pi} ln \left| \frac{\varphi_{An}}{\varphi_{An+1}} \right| \quad (1)$$

where $\varphi_{An} > \varphi_{An+1}$, φ_{An} and φ_{An+1} are the n-th and $(n + 1)$-th roll amplitudes (peaks or troughs), respectively.

In the experiment, the ship model with adjusted center of gravity and moment of inertia was placed in the towing tank, and its initial roll angle was given and released. The time series of decay motion was recorded, and then the natural period of roll and viscous damping coefficient were analyzed. Each group of tests was repeated three times, with a standard deviation of the results being less than 3%, and the final results were averaged.

(2) Zero-Speed White Noise Wave Model Tests

Experiments were carried out under head (180°), bow quartering (135°), and beam (90°) wave conditions in white noise waves with a simulated full-scale significant wave height of 2.1 m. The measurement contents include the six-degree-of-freedom motion response at the center of gravity of the ship, the three-dimensional acceleration of the center of gravity, legs, main/auxiliary crane rest positions, jacking case upper guides of leg, and helideck, and the relative wave surface elevation at the center of the leg. Finally, response amplitude operator (RAO) of each measuring point is obtained. The coordinates of each measurement position are shown in Table 2.

Table 2. Coordinate Positions of Measurement Points.

Measurement Location	Longitudinal Pos., m (from #0)	Transverse Pos., m (from Centerline, +ve Port)	Vertical Pos., m (from Baseline)
Center of Gravity	62.5	0	20.1
Main Crane Rest P1	109.9	5.85	32.5
Aux. Crane Rest P2	24	−27.3	28.0
Fwd. jacking case upper guide P3	97.7	−20.8	20.4
Aft. jacking case upper guide P4	22.5	12.15	20.4
Helideck P5	120	−20.8	29.5

(3) Irregular Wave Model Tests in Operational Sea States

The target operational sea state selected for this study has a significant wave height of 1.8 m, simulating transit operations within wind farm fields and dynamic positioning jack-up operations under full load conditions. In accordance with relevant regulations, the duration for each irregular wave test was 30 min at model scale, corresponding to 3 h for the full-scale vessel. Tested wave directions included head (180°), bow quartering (135°), and beam (90°) seas. The measured parameters encompassed the hull motion performance, the relative wave surface elevation at the leg positions, and the acceleration responses at typical locations. These measurements provide a basis for optimizing the platform design and verifying theoretical calculations.

The primary facilities of the towing tank included:

(1) Wave absorbers at the tank end and sides, which demonstrated effective wave absorption performance.

(2) A locally adjustable false bottom, allowing the water depth to be varied from 0 to 5 m.
(3) A towing carriage with a maximum speed of 9 m/s.
(4) A data acquisition and real-time analysis system.

The main instruments used in the tests were:

(1) A non-contact optical 6-DOF motion measurement system, used to measure the ship model's six-degree-of-freedom motions, with an uncertainty of <0.1° in rotation and <1 mm in displacement.
(2) Resistance-type wave probes, used to measure wave height and relative wave elevation at the legs, as shown in Figure 2a, with a measurement uncertainty of <0.1%.
(3) Tri-axial accelerometers were installed at the center of gravity, legs, crane, helideck, and other critical locations, as shown in Figure 2a, with a measurement uncertainty of <0.5%.
(4) Cameras and photographic equipment, used to document the testing process and support motion trajectory verification.

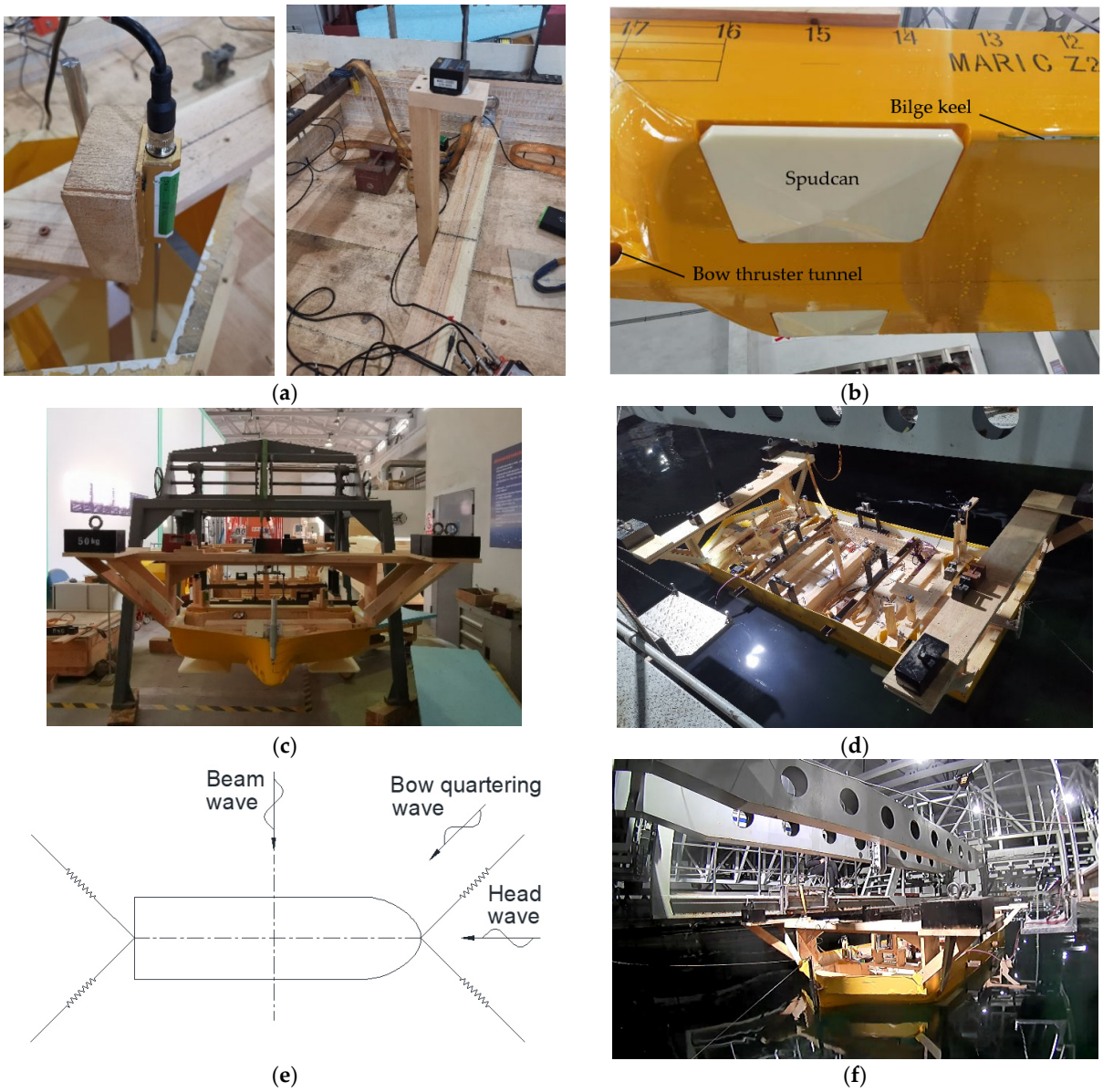


Figure 2. Model fabrication scheme and photographs. (**a**) Installation of wave gauges and accelerometers. (**b**) Installation of bilge keel and spudcan. (**c**) Photos of center of gravity and inertia adjustment. (**d**) Photo of the model arrangement in the tank. (**e**) Schematic diagram of the horizontal mooring system arrangement in the model test. (**f**) Photo of bow mooring line arrangement.

2.3. Test Model Construction

The vessel model is a wooden structure, and the appendages include the bow thruster tunnel, bilge keels, and dead wood, etc. Its shape is accurately processed according to the lines plan, as shown in Figure 2b. The ship model meets the geometric similarity conditions and the accuracy requirements of the test procedures. The displacement, center of gravity position, pitch and roll inertia radius are adjusted by configuring the internal ballast to make it consistent with the full-scale vessel state. The adjustment process of the center of gravity position and the inertial radius is shown in Figure 2c. The main particulars and related parameters of the WTIV are listed in Table 1.

During the seakeeping test, in order to suppress the drift of the ship model caused by the slow drift force of the wave and avoid it exceeding the capture range of the non-contact optical motion measuring instrument, the horizontal mooring system is used to limit the ship model. The system is composed of four flexible mooring lines, each of which is composed of 'thin steel wire + soft spring'. The mooring stiffness is reasonably designed to ensure that the wave-frequency motion response of the hull is not affected. The mooring points are symmetrically arranged on the height plane of the center of gravity of the ship model, two at the bow and two at the stern. The specific layout diagram is shown in Figure 2e,f. The overall layout of the ship model in the pool is shown in Figure 2d. Under the constraint of the horizontal mooring system, the natural period model values of the surge, sway and yaw motions of the ship model are all greater than 15 s, which is much larger than the experimental wave period range (0.9–4.0 s), thus effectively avoiding coupling interference.

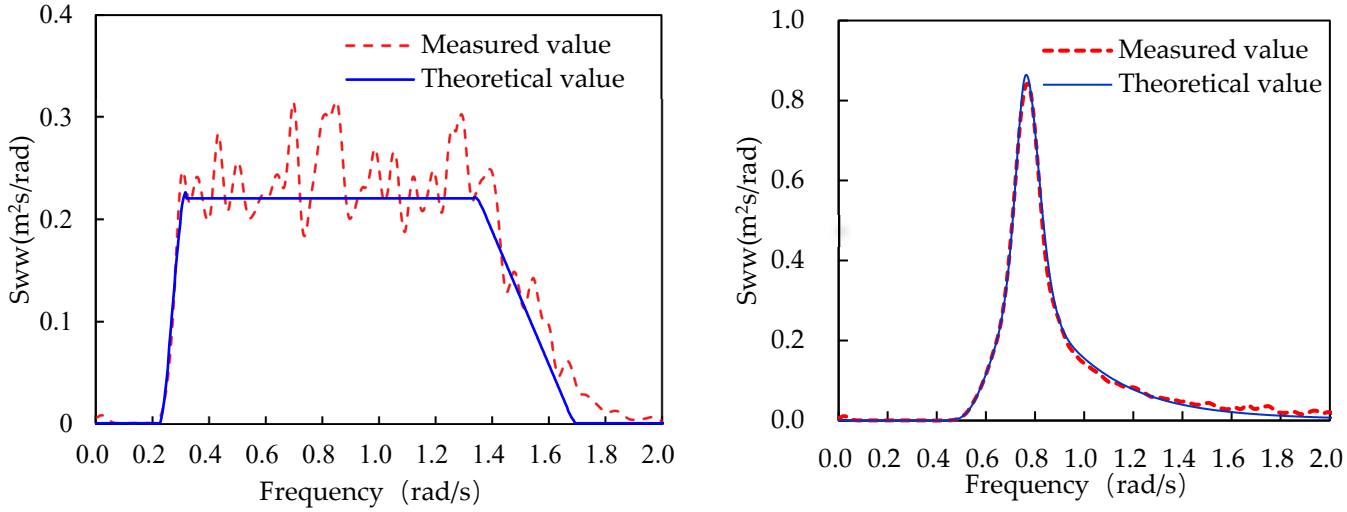
2.4. Wave Simulation

In this study, waves were simulated using the wavemaker at the head of the large towing tank. The simulated wave conditions included white noise waves and irregular waves representing operational sea states. Based on the target wave spectrum, corresponding white noise and irregular wave time series were generated. Prior to formal testing, wave calibration was conducted in the basin to ensure that the spectra of the generated white noise and irregular waves matched the shape of the target spectrum. During testing, a resistive wave gauge was installed at a position corresponding to the center of gravity of the WTIV model.

White noise waves are characterized by a broad spectrum and irregularity. Within the frequency range of interest for this experimental study, the spectral density function of the generated white noise waves approximated a straight line. Consequently, a single model test in white noise waves can substitute for a series of tests in regular waves. In practice, high-frequency and low-frequency cut-offs were applied to the white noise spectrum according to the wavemaker's capabilities. Due to the poor quality of wave generation near these cut-off frequencies, transition zones were typically implemented. The effective low-frequency cut-off of the wavemaker used in this experiment was 1.256 rad/s (corresponding to a period of 5 s), and the high-frequency cut-off was 12.56 rad/s (corresponding to a period of 0.5 s). Therefore, the frequency range from 1.8 rad/s to 8 rad/s, which encompasses the peak energy range commonly encountered in model tests, was selected as the flat section of the spectrum. Transition sections were defined from 1.4 rad/s to 1.8 rad/s (rising) and from 8 rad/s to 10 rad/s (falling). Thus, the target spectrum for the white noise waves used in the model tests was a trapezoidal polyline.

According to the relevant test experience and considering the large displacement of the test model, the model value of the significant wave height of the white noise wave is 6 cm, and the corresponding full-scale significant wave height is 2.10 m. The significant wave height and the zero-order moment of the spectral density, m_0 (the area under the spectral

density curve), satisfy the relationship $H_s = 4\sqrt{m_0}$, so the spectral density value of the straight section of the spectrum can be determined to be 0.22 $m^2 \cdot s/rad$. Before the model test, the wave time history is checked based on the white noise target spectrum. Figure 3a shows the comparison between the measured spectrum and the target spectrum in the white noise irregular wave model test, indicating good overall agreement between the measured and theoretical spectra. The Root Mean Square Error (RMSE) value is 0.0126 $m^2 \cdot s/rad$, and the percentage difference is generally less than 10% within the effective frequency range, demonstrating that the wave generation system can accurately simulate the white noise characteristics. According to the relevant ITTC specifications, the duration of each test of the model in white noise irregular waves is 10 min, and the wave sampling frequency is 50 Hz.



(**a**) White noise wave. (**b**) Irregular waves in operational sea conditions.

Figure 3. Comparison of measurement spectra and target spectra.

The JONSWAP wave spectrum was used to simulate the platform's operational sea state. The environmental parameters for the operational sea state simulated in the tests are shown in Table 3.

Table 3. Operational sea state JONSWAP wave spectrum parameters.

Peak Enhancement Factor γ		**Significant Wave Height H_s (m)**		**Peak Period T_P (s)**	
Full-Scale	Model test	Full-Scale	Model test	Full-Scale	Model test
1.0	1.0	1.80	0.051	8.21	1.39

The expression for the JONSWAP wave spectrum is given by

$$S(f) = \alpha H_s^2 \frac{1}{T_p^4 f^5} exp\left[-\frac{5}{4}\left(\frac{1}{T_p f}\right)^4\right] \gamma^{exp[-\frac{(T_p f-1)^2}{2\sigma^2}]} \tag{2}$$

$$\alpha = 0.0624/\left[0.23 + 0.0336\gamma - 0.185(1.9+\gamma)^{-1}\right] \tag{3}$$

where H_s is the significant wave height, T_p is the peak period, f is the wave frequency (Hz), γ is the peak enhancement factor, and σ is the shape parameter, which takes the following values:

$$\sigma = \begin{cases} 0.07, & f \le f_p \\ 0.09, & f > f_p \end{cases} \tag{4}$$

For the irregular wave simulation of operational sea conditions, the sampling frequency is set to 20 Hz and the sampling time is 30 min (corresponding to 3 h of full-scale ship). Starting from the issuance of wave-making instructions, after the model fully interacts with the wave, the sampling record is started. Figure 3b presents the comparison between the target spectrum and the measured spectrum for the simulated irregular waves, showing good overall matching for the JONSWAP wave spectrum simulation. The RMSE value is 0.0143 $m^2 \cdot s/rad$, and the percentage difference is below 5% in the peak region. The difference in the spectral peak is only 2.66%, confirming that the wave generation system accurately captures the shape of the JONSWAP spectrum and verifying the reliability of the wave simulation.

3. 3D Numerical Towing Tank Simulation Method Based on CFD

The numerical prediction methods of ship seakeeping mainly include Potential Flow Theory and Viscous Flow Theory. The potential flow theory has the core advantage of high computational efficiency and is suitable for the prediction of frequency domain motion response in the preliminary design stage of ships. However, it is difficult to accurately simulate the physical phenomena dominated by viscosity (such as roll damping and vortex-induced vibration) based on the linear assumption. Especially when solving the roll motion, due to the significant influence of the viscous load (especially the vortex generation effect), the prediction accuracy may be seriously reduced by relying solely on the potential flow theory. In contrast, the viscous flow theory has more advantages in terms of physical authenticity and can accurately capture nonlinear waves and fluid-solid coupling effects, but its computational cost is high, and it needs to be weighed between grid resolution and computational resources.

In order to fully consider the influence of fluid viscosity (especially the vortex effects generated at the hull's bilge corners and appendage areas) on roll damping and motion response, this paper uses CFD numerical pool simulation technology based on viscous flow to calculate the hull motion response under the action of hydrostatic roll damping and irregular waves.

3.1. Numerical Wave Generation Theory

To effectively control the amplitude, direction and frequency of waves and improve the convergence and efficiency of calculation, the numerical tank uses the Boundary Wave Generation method to generate waves. Based on the analytical solution of wave theory, the method directly generates waves by specifying the fluid velocity and volume fraction at the inlet boundary. The core of the method is to combine the Navier–Stokes equation with Volume of Fluid (VOF) multiphase flow model to apply the analytical velocity field and wave surface equation of the wave at the boundary.

3.2. Numerical Wave Absorption Method

Wave absorption aims to suppress reflected waves at the outlet boundary. The common method is to add an artificial damping source term in the area near the exit and dissipate the wave energy through the negative feedback term in the momentum equation to simulate the non-reflective boundary. Euler Overlay Method (EOM) is the core technology of Wave Damping in STAR-CCM+. The method combines overlapping grid technology, damping function construction and modified Navier–Stokes equation and introduces artificial damping term in the outlet region to suppress wave reflection. The wave attenuation zone is usually located near the outlet boundary, and the wave energy is dissipated by adding the damping source term S_d to the momentum equation to prevent the

reflected wave from interfering with the flow field. In this region, the continuity equation and momentum equation are modified as:

$$\frac{\partial \rho}{\partial t} + \nabla \cdot \left(\rho \vec{u} \right) = 0 \tag{5}$$

$$\frac{\partial \left(\rho \vec{u} \right)}{\partial t} + \nabla \cdot \left(\rho \vec{u} \otimes \vec{u} \right) = -\nabla p + \nabla \cdot \tau + \rho g + S_d \tag{6}$$

$$S_d = -\mu(x)(\vec{u} - \vec{u}_{target}) \tag{7}$$

$$\mu(x) = \mu_{max} \cdot \left[1 - cos\left(\pi \frac{x - x_0}{x_e - x_0} \right) \right], x_0 \leq x \leq x_e \tag{8}$$

where ρ is the fluid density, $\vec{u}$ is the velocity vector of the fluid particle, p is the hydrostatic pressure, τ is the viscous stress tensor, g is the gravitational acceleration vector, $\mu(x)$ is the position-dependent damping coefficient, which increases gradually from 0 to a maximum within the damping zone. $\vec{u}_{target}$ is the target velocity (usually the still water velocity or zero); x_0, x_e are the start and end positions of the damping zone, respectively; μ_{max} is the maximum damping coefficient (related to the wave period T).

When solving the Navier–Stokes equations, the governing equation for an arbitrary physical quantity based primarily on the Finite Volume Method (FVM) is [23]:

$$\frac{\partial}{\partial t} \int_V \rho \varnothing dV + \oint_S \rho \varnothing \vec{u} \cdot dS = \oint_S \Gamma_\varnothing \nabla \varnothing \cdot dS + \int_V S_\varnothing dV \tag{9}$$

where $\Gamma_\varnothing$ is the diffusion coefficient for the physical quantity $\varnothing$, $S_\varnothing$ is the source term, S is the surface area of the control volume, and dS is the surface normal vector (positive outward).

3.3. Free Motion Governing Equations

In this paper, the Dynamic Fluid Body Interaction (DFBI) method is used to simulate the hull motion caused by the force and moment of the fluid acting on the hull surface [24]. The motion is applied to the hull surface and the entire overlapping grid area. DFBI motion was simulated with only two degrees of freedom, heave and pitch, that is, to solve the motion problem of two-dimensional degrees of freedom. The governing equations of heave and pitch are [25]:

$$F_Z = \mathrm{m} \frac{d^2 z_{cg}}{dt^2} \tag{10}$$

$$M_Y = \frac{d}{dt^2} \left(I_Y \frac{d\theta}{dt} \right) \tag{11}$$

$$m\left(\dot{\omega} - \dot{\theta} u \right) = F_Z - D_h \omega \tag{12}$$

$$I_Y \ddot{\theta} = M_Y - D_p \dot{\theta} \tag{13}$$

where F_Z and z_{cg} are the resultant external force and displacement along the Z-axis for the hull, respectively; m is the hull mass; M_Y and I_Y are the pitch moment and moment of inertia about the Y-axis for the hull, respectively; $\dot{\omega}$ is the heave acceleration; $\dot{\theta}$ and $\ddot{\theta}$ are the pitch angular velocity and acceleration, respectively; u is the hull speed in the X-axis direction; and D_h and D_p are the additional damping coefficients for heave and pitch,

respectively, taken as 0.1 in this study [22]. After the software iteratively computes for three wave periods, the calculation residuals and various monitoring data tend to stabilize.

3.4. Static Water Roll Damping Calculation Model

This study conducts CFD analysis on the static water roll characteristics of the WTIV under different leg deployment lengths (normal transit condition: 0 m; DP/jack-down conditions: 5 m, 10 m, 20 m). The calculation model is consistent with the model test. The full-appendage model is adopted, including the structure of the bow thruster tunnel, bilge keels, spudcans, and stern deadwood. The 1:35 scale ratio is selected for simulation in STAR-CCM + software (version 2210).

Using the overlapping grid method, the fluid domain is divided into an overlapping grid area and a background grid area moving with the ship, as shown in Figure 4a. The boundary conditions are set as follows: the ship head forward 1.5 times L_{wl}, the water surface downward 1.5 times L_{wl}, and the water surface upward 0.5 times L_{wl} is set as the speed entrance; the stern backward 1.5 times L_{wl} is set as the pressure outlet; the middle longitudinal section is set to a symmetrical plane at 4 times the ship width on the left and right sides. In the overlapping grid area, the hull surface is set as a Smooth No-slip Wall, and the rest of the surface is an Overset Mesh.

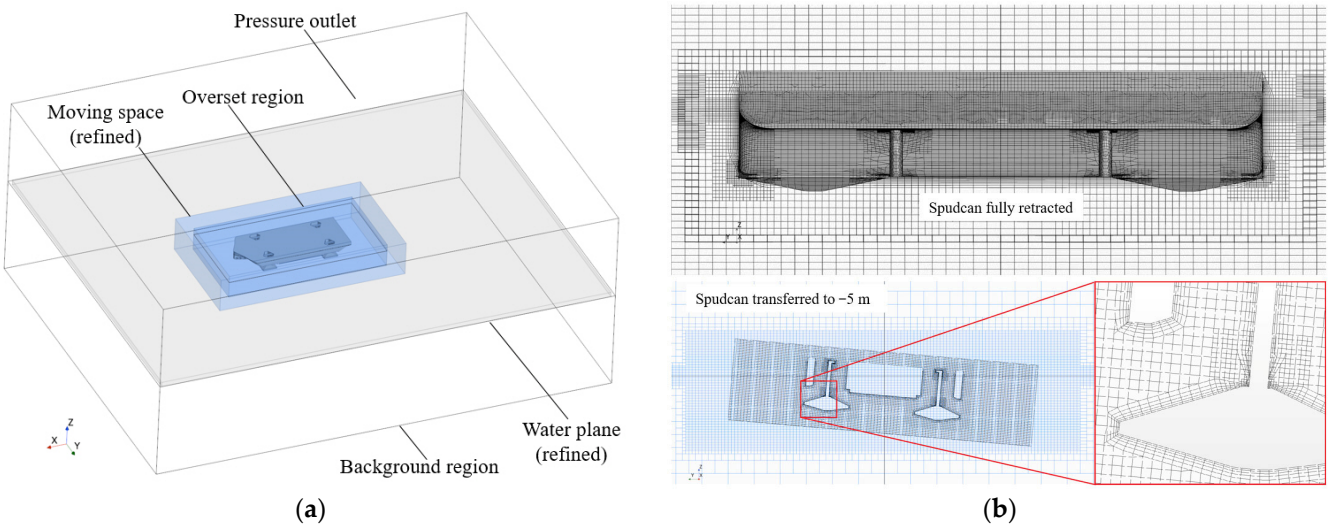


Figure 4. Computational domain and mesh profile. (**a**) Division of computational fluid domain in numerical simulation. (**b**) Local mesh refinement of spudcan and appendage surfaces.

The Trimmed Cell [24] mesh method is used, discretizing the computational domain and boundaries with hexahedral structured grids. The prism layer grid is arranged near the hull surface, and the basic grid size is 0.12 m. The hull surface mesh is controlled in the range of 3.75–30 mm according to the curvature change. Five prism layers are set on all surfaces except the deck. The thickness of the first grid layer near the wall is about 2.5 mm, the growth rate of the prism layer is 1.3, and the total thickness is 23 mm. The grid size of the moving space in the overlapping grid area and the background grid is 37.5 mm × 37.5 mm × 18.75 mm. In order to accurately simulate the wave, the grid is refined in the wave region, and the size is set to 30 mm × 30 mm × 15 mm. The results of mesh size convergence analysis, as shown in Table 4, indicate that the mesh density meets the requirements for convergence and computational deviation (<5%). The remaining regional grids gradually transition from the hull surface to the outside, and the final number of overall grids is about 6.4 million. When the legs are fully retracted or deployed to different lengths, local mesh refinement is applied to the appendage areas such as the

spudcans, well structures, and deadwood. Figure 4b gives the grid division when the leg is lowered by 5 m.

Table 4. Analysis of the mesh size convergence.

Mesh Size (mm)	Roll Period, T (s) Compare to Experimental Value (2.87 s)		Critical Damping, μ Compare to Experimental Value 0.0504	
	CFD Value	Deviation (%)	CFD Value	Deviation (%)
60.0	3.35	16.7	0.056	11.1
42.5	3.11	8.36	0.053	5.16
30.0	2.98	3.83	0.049	−2.78
22.5	3.00	4.53	0.050	−0.79

The DFBI method was used to solve the forces and moments acting on the hull from the fluid, obtaining the ship's motion state through iterative calculation. Convergence analysis with four different time steps (as shown in Table 5 below) demonstrates that the time step adopted in this numerical study satisfies convergence requirements. Consequently, a time step of 8.0 ms (with a computational error < 5%) was selected for the simulations. The temporal discretization employs a second-order scheme, and the maximum number of iterations is set to 10. The physical model is set as follows: Implicit Unsteady is selected as the time term; the VOF method is selected for the multiphase flow model. The viscous model adopts the SST k-ω turbulence model based on RANS. The simulation allowed freedom in roll and heave for the model. The model was initially given a 5° starboard inclination about the center of flotation in calm water and then released to roll freely.

Table 5. Analysis of the Time step convergence.

Time Step (ms)	Roll Period, T (s) Compare to Experimental Value (2.87 s)		Critical Damping, μ Compare to Experimental Value 0.0504	
	CFD Value	Deviation (%)	CFD Value	Deviation (%)
15.0	3.33	16.03	0.047	−6.75
11.0	3.11	8.36	0.048	−4.76
8.0	2.98	3.83	0.049	−2.78
6.0	2.99	4.18	0.048	−4.76

3.5. Motion Response Calculation Model

In this paper, the WTIV motion response under the action of JONSWAP wave spectrum (parameters are shown in Table 3) is simulated and calculated. Due to the first oblique wave and transverse wave conditions, the whole ship model is used instead of the half ship model. The top, bottom, inlet and side of the numerical tank are set as symmetrical boundary conditions, and the outlet is set as pressure outlet. The front, back, left and right boundaries of the background grid domain are processed by EOM, and the length of the wave elimination zone is 1.2 m.

Overlapping grid division is shown in Figure 4a. The cutting body mesh method is used to discretize the computational domain and boundary by hexahedral structured mesh. The prismatic layer mesh is arranged near the hull surface, and the basic mesh size is 0.15 m. The hull surface mesh is controlled in the range of 4.7–37.5 mm with the change in curvature, and the prism layer mesh is set except the deck surface. The thickness of the first layer of the prism layer near the wall is about 1.1 mm. In order to ensure the smooth transition between the outermost layer of the prism layer and the overlapping grid area, a total of 10 layers of prism layer grids are set up, with a growth rate of 1.2 and a total

thickness of 30 mm. The grid size of the overlapping grid area and the moving area in the background grid is 37.5 mm × 37.5 mm × 18.75 mm. In order to accurately simulate the wave, the mesh is refined in the wave area. The mesh size is set to 18.75 mm × 18.75 mm × 4.7 mm, which is about 1/22 of the maximum wave height. The remaining regional grids gradually transition from the hull surface to the outside, and the final number of overall grids is about 7.3 million.

The model test duration is 30 min, corresponding to a calculation time of approximately 1800 s for the ship motion response in irregular waves under the three wave directions in the CFD simulation.

4. Results and Discussion

4.1. Roll Damping Characteristics Analysis of WTIV

4.1.1. Benchmark Condition Validation

The results of the comparison between the model test and the CFD simulation are shown in Table 6. It can be seen from the table that the roll natural period and damping coefficient obtained by CFD simulation are highly consistent with the model test results (error < 5%), which verifies the reliability of the numerical method and reveals the following phenomena:

(1) The wave has been fully dissipated before reaching the boundary, with no signs of reflected waves. The peak spacing (about 3.0 m) is significantly smaller than the theoretical wavelength (about 12.6 m) calculated based on the roll period, indicating that the radiation wave generated by the hydrostatic roll free decay test is a short-term transient wave, rather than a continuous gravity wave. The change in free surface wave height is shown in Figure 5a.

(2) The vortex is generated at the downstream side of the bilge corner, promptly detaches from the hull during the roll process, and develops in the near-field region. Due to the small size of the bilge keel of the ship, the generated vortices are not particularly strong. Figure 5b shows the evolution of the flow field at the hull's mid-ship section and the bilge keel area during a roll cycle.

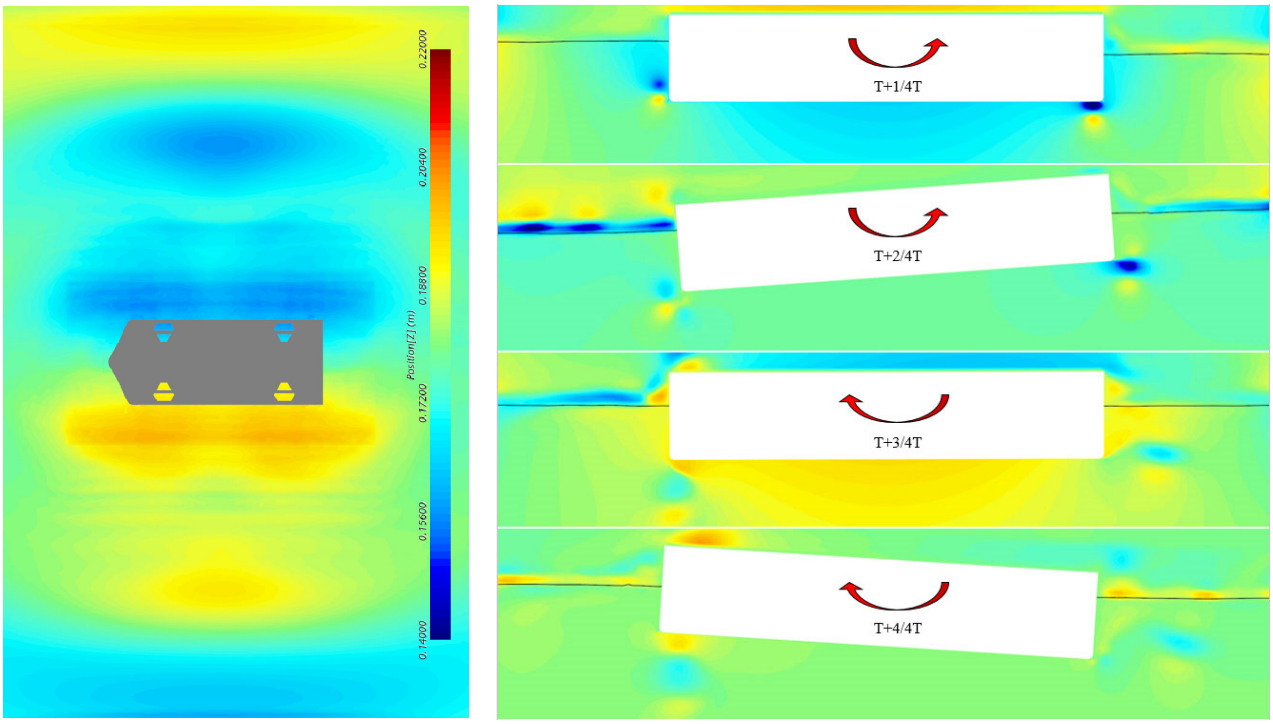
(3) The CFD results in the first two cycles are basically consistent with the experimental data. Starting from the third cycle, a phase difference between the CFD and test results gradually emerges. As time progresses, the phase error accumulates, and the amplitude decay rate in the CFD simulation is faster than that of test. The free decay curves of roll in still water are shown in Figure 6. The average decay rates from the CFD predictions and model test results are 0.8972 and 0.9176, respectively, with a difference of 0.0205 (corresponding to approximately 2.23%). The RMSE of the peak points is 1.1194 deg, mainly due to the difference in the initial roll angle.

4.1.2. Leg Laying Down Condition Analysis

Based on the above analysis, the CFD method and process used in this paper meet the calculation accuracy requirements of WTIV damping coefficient and roll period. On this basis, the CFD prediction of the roll period and damping coefficient of the platform is carried out for the different positions (−5 m,−10 m and −20 m) of the leg in the DP operation. The results of the rolling free decay test of the WTIV in still water are given in Figure 6. According to Formula (1), the roll period and damping coefficient corresponding to different leg lowering positions are obtained, as shown in Table 7 and Figure 7. The comparison results show that the damping coefficient increases linearly with the increase in leg depth (Case_5 to Case_20), which is consistent with the theoretical prediction by Byrdal et al. (2024) [18].

The physical mechanism is that, as the depth of the leg increases, the VCG of the hull center of gravity decreases, and the metacentric height (GM) increases, leading to a

shorter roll period. At the same time, the abrupt geometric change at the corner structure in the spudcan and the well area causes flow separation, generating significant vortices. As shown in Figure 8, a symmetrical double-vortex structure forms, particularly in the wake region of the spudcan sectional corner. When the hull rolls to a specific phase, these vortices shed from the hull, migrate into the near field, and eventually dissipate due to turbulent viscosity. This phenomenon aligns with the findings of Gao et al. (2019) [19] and Ding et al. (2022) [20].



(**a**) (**b**)

Figure 5. (**a**) Free surface elevation for the benchmark condition (Case_0), captured at 3.2 s after the start of decay. (**b**) Contour of flow velocity evolution during one complete roll cycle from the CFD model scale simulation.

Table 6. Comparison of CFD numerical calculations and model test results for roll period and damping coefficient.

Item	Model		Full Scale		Error
	Experiment	CFD	Experiment	CFD	
Period (s)	2.87	2.98	16.98	17.63	3.83%
Damping Coeff.	0.0504	0.049	0.0504	0.049	−2.78%

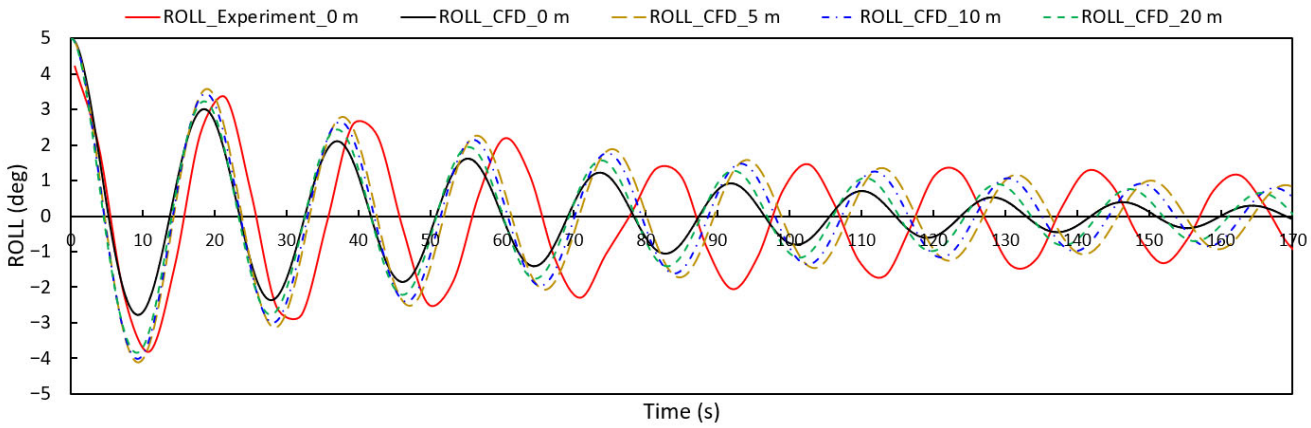


Figure 6. Time history curve of free roll decay.

Table 7. Prediction results of WTIV roll period and damping coefficient under different leg laying down positions.

Case	Spudcan Location (m)	VCG (m)	Damping Coefficient, μ	Roll Natural Period T_CFD
Case_0	0	20.1	0.049	17.630
Case_5	−5	19.2	0.033	18.789
Case_10	−10	18.2	0.035	18.627
Case_20	−20	16.4	0.039	18.418

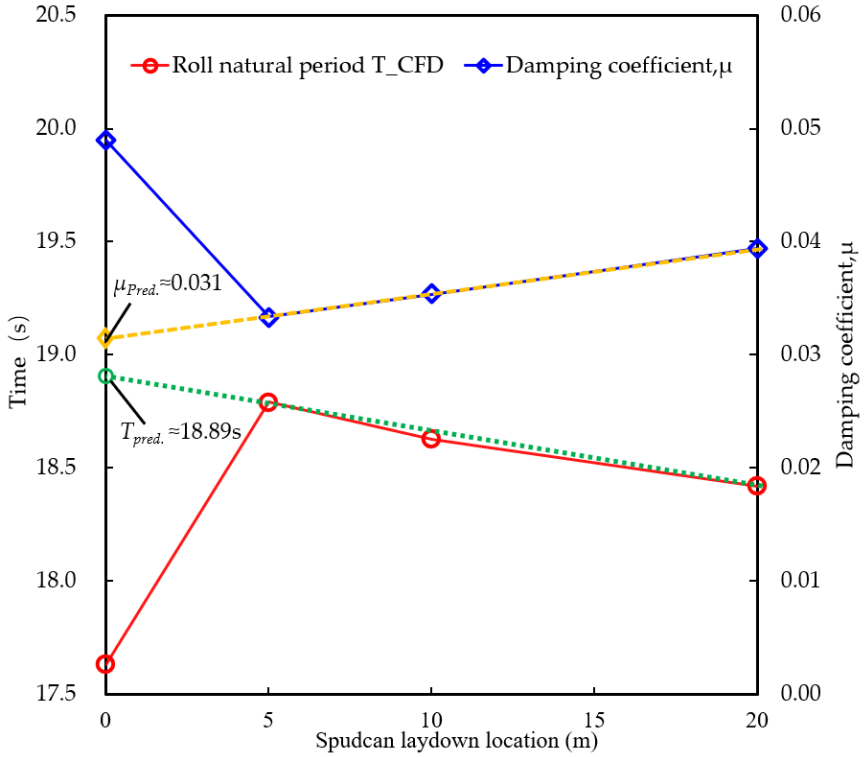


Figure 7. Comparative analysis schematic diagram of numerical prediction results for WTIV roll period and damping coefficient.

The process of vortex generation, transport, and dissipation alters the distribution of the normal pressure gradient on the structural surface, thereby significantly enhancing the hull's viscous roll damping. Furthermore, as the leg penetration depth increases, the flow velocity around the spudcan tip rises, intensifying vortex dissipation and consequently

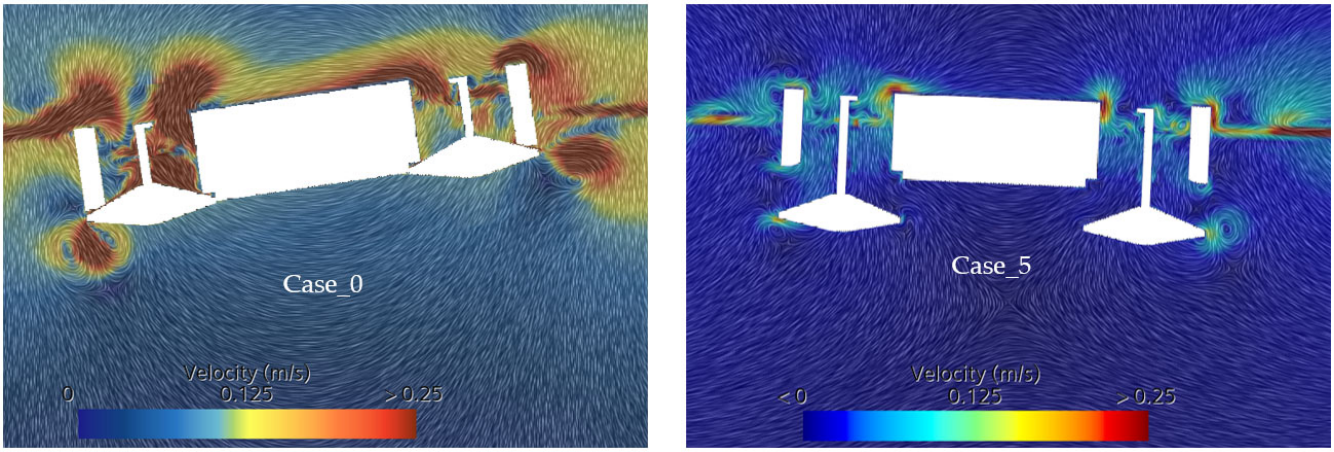
increasing the roll damping coefficient—a trend consistent with the similarity criterion proposed by Lei et al. (2023) [21].

A comparison between Case_0 and Case_5 reveals an anomalous phenomenon: although the vertical center of gravity (VCG) in Case_0 is significantly higher than in Case_5, its roll period is shorter and its roll damping coefficient is substantially larger. This indicates that, at the same draft, fully retracting the legs into the wells leads to an abrupt change in the roll damping and period of the WTIV.

In order to further analyze this abnormal phenomenon, Figure 9 shows the free surface change and velocity distribution of the water line surface of the spudcan trap and its adjacent area (taking the leg laying down 5 m as an example) in Case_0 and Case_5 single rolling cycle. The specific analysis is as follows:

(1) In Case_0 (spudcans fully retracted), fluid exchange between the well and the exterior is restricted. This results in a higher liquid level inside the starboard well than the external free surface, with the opposite occurring on the port side. The fluid inside the well generates a counterclockwise restoring moment, which significantly counteracts the port-side rolling tendency. Consequently, the well structure in Case_0 functions similarly to a free-flooding anti-roll tank, shortening the roll period by approximately 7% and increasing the roll damping by about 58%—even exceeding the damping achieved in Case_5, which has a lower center of gravity.

(2) In Case_5 (spudcans lowered 5 m), the opening to the sea is sufficiently large, allowing rapid fluid exchange between the well and the exterior. The free liquid surfaces inside the port and starboard wells remain largely level with the external sea surface. As a result, the anti-rolling effect of the well structure diminishes, and the roll damping becomes significantly lower than in Case_0.



(**a**) Case_0 (**b**) Case_5

Figure 8. Flow velocity and vortex distribution.

To quantify the influence of the liquid in the wells on the roll period and damping, based on the roll differential equation, the hull roll period can be expressed as:

$$T = 2\pi\sqrt{I'_{XX}/\Delta \cdot g \cdot \overline{GM}} \tag{14}$$

From this, the additional moment of inertia ΔI_{XX} for Case_0 can be obtained as:

$$\Delta I_{XX} = I'_{XX} - I_{XX} = \frac{\Delta \cdot g \cdot \overline{GM} T^2}{(2\pi)^2} - \Delta \cdot R_{XX}^2 = 1.57 \times 10^7 tm^2 \tag{15}$$

At the same time, since the wells are standard geometric structures with fixed positions, the additional moment of inertia $\Delta I'_{XX}$ of the four well liquid tanks relative to the ship's center of gravity can be calculated according to the initial liquid level height (i.e., draft) using the following formula:

$$\Delta I'_{XX} = \sum \left\{ m_i \left[{y_i}^2 + (z_i - z_T)^2 \right] + I_i \right\} = 1.56 \times 10^7 t m^2 \approx \Delta I_{XX} \quad (16)$$

where Δ is the ship displacement (t); $\overline{GM}$ is the initial metacentric height corrected for free surface effect (m); T is the natural roll period obtained from the test (s); I'_{XX} is the total moment of inertia for Case_0; I_{XX} is the moment of inertia without considering the liquid in the leg−spudcan wells (t·m^2); R_{XX} is the roll radius of gyration (m); m_i is the liquid mass in a single spudcan well tank (t); y_i and z_i are the transverse and vertical coordinates of the center of gravity of this liquid tank, respectively (m); I_i is the moment of inertia of a single well tank (t·m^2); and z_T is the vertical height of the ship's center of gravity (m).

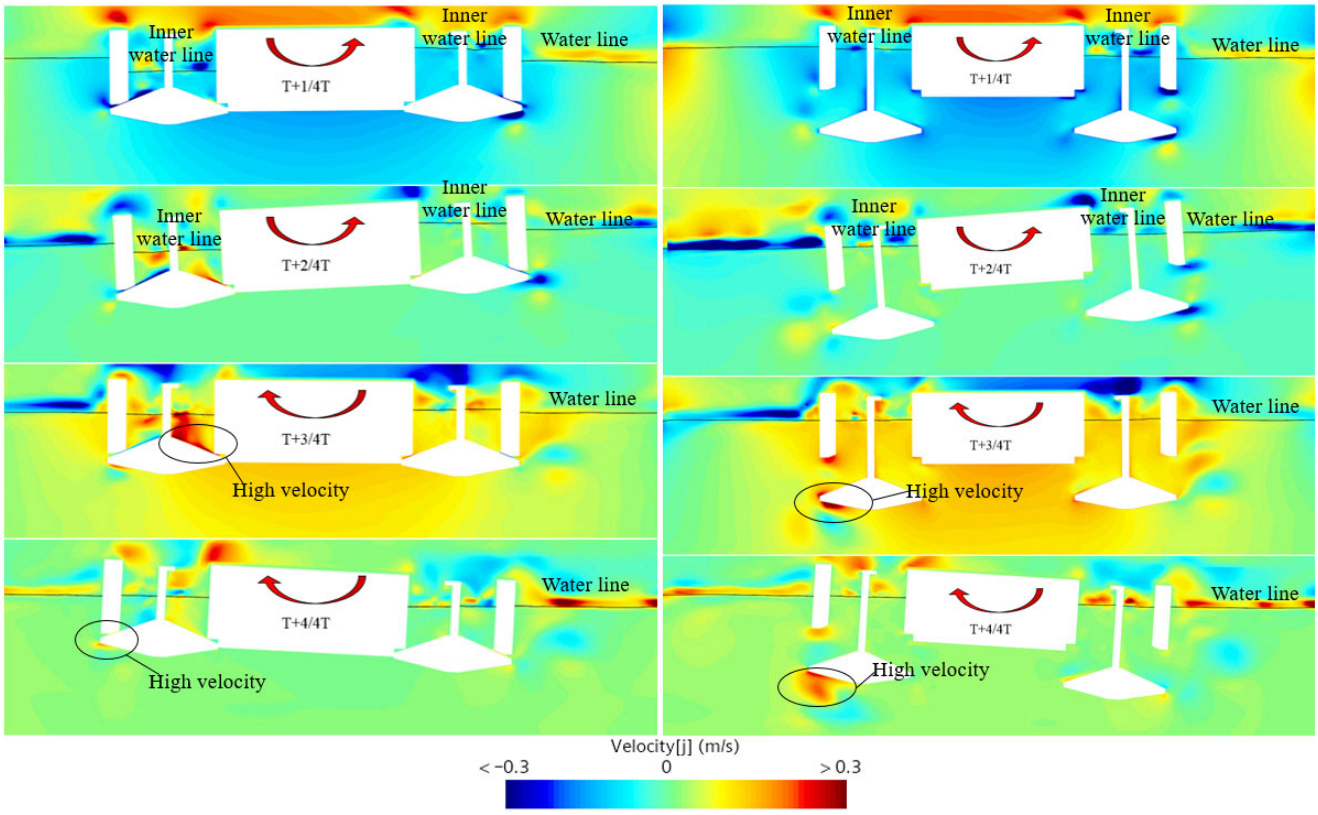


Figure 9. Velocity distribution at the waterline plane and its adjacent areas in the cross-section of the leg-spudcan well.

Comparing the above calculation results, it is evident that this anomalous phenomenon is primarily caused by the free-flooding anti-roll tank effect of the well areas. Quantitative analysis using Equations (14)–(16) confirms that it originates from the additional moment of inertia ($\Delta I'_{XX} \approx \Delta I_{XX}$) generated by the liquid in the wells. The strength of this effect is proportional to the ship's draft and the product of the liquid mass m_i in the leg-spudcan well region and the square of the distance y_i from its center of gravity to the ship's centerline. The related quantitative assessment method is universally applicable to WTIVs equipped with leg-spudcan well structures.

4.2. Motion Response Characteristics of WTIV

4.2.1. Characteristics of RAO

In this paper, the time history curve of the six-degree-of-freedom motion response of the ship model is obtained by white noise test. By using the fast Fourier transform (FFT) method, the motion time history is transformed into the response spectrum S_A (ω), which is divided by the input white noise spectrum S_{WV} (ω) to obtain RAO of the six-degree-of-freedom motions of the ship model:

$$RAO = H(\omega) = \sqrt{S_A(\omega)/S_{WV}(\omega)} \quad (17)$$

Due to space limitations, this paper only gives the comparison of RAO between the ship model tests and the numerical prediction under the conditions of head (180°), bow quartering (135°), and beam (90°) wave conditions at the center of gravity of the ship and the main crane boom rest P1, as shown in Figure 10.

Under the same measurement position and different wave directions, the RAO of WTIV shows the following rules: The maximum response for roll angle and transverse acceleration occurs in bow quartering seas, followed by beam seas [Figure 10a]; the pitch angle response and longitudinal acceleration are greatest in head seas, followed by quartering seas [Figure 10b]; and the heave motion and vertical acceleration show the largest response in beam seas, decreasing in bow quartering and head seas, respectively [Figure 10c].

The change law of WTIV motion response transfer function under the same wave direction and different spatial positions is as follows: the horizontal acceleration increases with the increase in the height of the measuring point [Figure 10d]; the response value increases when the vertical acceleration is far away from the ship [Figure 10e].

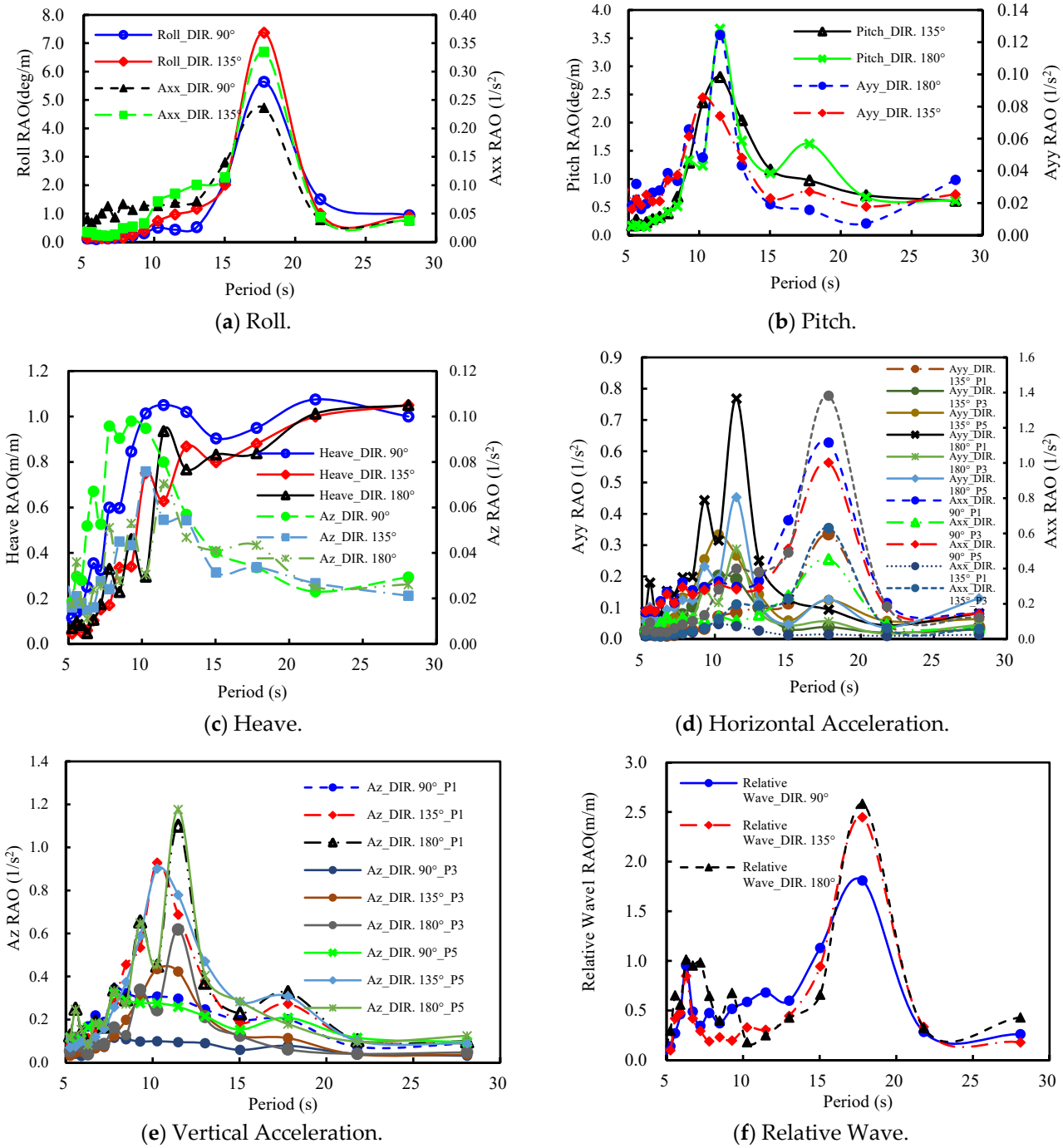


Figure 10. RAO curves of motion response transfer functions under different wave directions.

The above response peaks all occur near the corresponding roll period (about 17.8 s), pitching period (about 11.5 s) and heaving period (10–10.5 s), indicating that there is a significant resonance effect between the natural period of ship motion and the encounter wave period. Therefore, in the planning of WTIV main dimensions and loading scheme, the wave period characteristics of the operational sea area should be fully considered.

4.2.2. Irregular Wave Response Validation

In the operating sea state, the motion of the three degrees of freedom of surge, sway and yaw is mainly composed of low-frequency slow drift components, and its response is significantly affected by the stiffness and pretension of the horizontal mooring system. Therefore, the motion results of these three degrees of freedom in the irregular wave test

have limited practical reference significance. Table 8 presents a comparison of the heave, roll, and pitch motion responses of the WTIV under irregular wave conditions, as obtained from model tests and CFD calculations (converted to full scale). Additionally, predictions based on potential flow theory are included, providing the maximum undamped roll response at heading angles of 90° and 135°. The results indicate good agreement between the model test data and CFD calculations. However, the potential flow theory predictions, which do not account for damping, are approximately 13% lower than the model test values, with an estimated damping-related error in the range of 20–30%.

Table 8. Statistical Results of Ship Motion in Irregular Wave Tests (full scale).

Wave Dir.	Motion	Significant Value		1/100th Value		1/1000th Value		
		Experiment	CFD	Experiment	CFD	Experiment	CFD	PFM
180°	Heave (m)	0.28	0.24	0.41	0.38	0.43	0.40	-
	Pitch (°)	0.72	0.73	1.15	1.15	1.19	1.19	-
135°	Heave (m)	0.26	0.28	0.41	0.41	0.44	0.43	-
	Pitch (°)	0.81	0.95	1.49	1.48	1.72	1.63	-
	Roll (°)	0.42	0.41	0.73	0.73	0.80	0.76	0.91
90°	Heave (m)	0.48	0.48	0.78	0.81	0.89	0.88	-
	Roll (°)	0.43	0.48	0.73	0.79	0.86	0.86	0.97

It can be seen from the results that the target ship has the largest heave motion amplitude (0.89 m) under beam sea conditions, which further verifies the trend reflected in the RAO curve from the white noise tests. When the wave direction is 135° (bow quartering seas), the largest amplitudes of roll and pitch motion are 0.80° and 1.72°, respectively. This wave-induced hull motion may cause the legs and spudcans to experience seabed impact loads during DP and jack-down operations, as illustrated in Figure 11. According to the conservative analysis criteria of DNV (2015) [3], the analysis of such conditions should focus on the impact between the leg and the rigid seabed. For a platform without roll and pitch damping devices, the leg–seabed relative impact force is calculated based on the following conservative assumptions:

(a) Only a single leg is in contact with the seabed;
(b) All impact energy is absorbed by a single spudcan-leg-jacking system;
(c) The instantaneous motion of the spudcan is arrested, and the seabed is considered an infinitely rigid body (i.e., the actual geological characteristics of rock, sand, or clay are ignored).

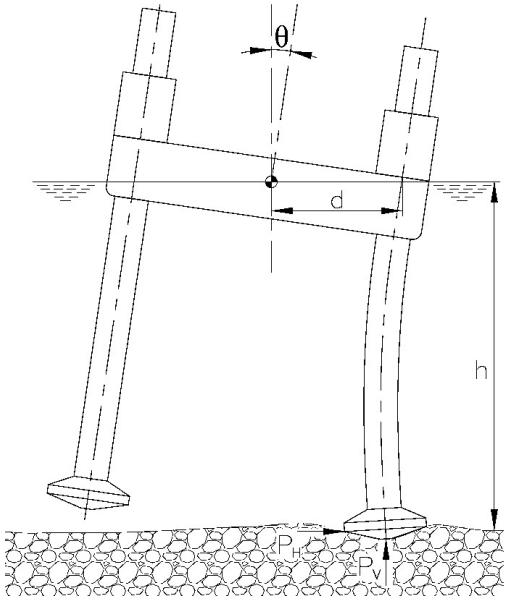


Figure 11. Schematic diagram of the impact load between the spudcan and the seabed bottom.

The maximum lateral and vertical impact forces are calculated using the following formulas:

$$P_{H,max} = 2\pi \cdot max\left(\frac{\theta}{T_{Roll}}\right)\sqrt{\frac{I_m k_H}{1+\frac{k_V}{k_H}\left(\frac{d}{h}\right)^2}} \tag{18}$$

$$P_{V,max} = 2\pi \cdot max\left(\frac{\theta}{T_{Pitch}}\right)\sqrt{\frac{I_m k_V}{1+\frac{k_H}{k_V}\left(\frac{h}{d}\right)^2}} \tag{19}$$

where k_H, k_V are the comprehensive lateral and vertical stiffness of the leg system (including spudcan−seabed interaction jacking system constraints), respectively (N/m); I_m is the platform's roll/pitch moment of inertia, considering added mass effects (kg·m^2); T is the platform's roll/pitch motion period (s); and θ is the platform's roll/pitch amplitude (rad).

From the above equations, it can be seen that the impact load on the leg and spudcan is primarily related to the hull motion parameter $max(\theta/T)$ values under different wave conditions can be obtained using the CFD method presented in this paper, thereby providing design extremes for spudcan and leg loads during DP jack-down and leg retrieval operations.

Based on the results of the test and CFD numerical prediction, the maximum value of the vertical acceleration (VAcc.) and its corresponding wave direction at six typical positions of the hull under the irregular wave operation sea condition are shown in Table 9.

Table 9. Maximum vertical acceleration under working sea conditions and its corresponding wave direction (m/s^2).

Location	Significant Value	1/100th Value	1/1000th Value	Maximum Value	Wave Direction
Center of Gravity	0.074	0.128	0.138	0.162	90°
Main Crane Rest P1	0.361	0.623	0.676	0.683	135°
Aux. Crane Rest P2	0.285	0.467	0.515	0.561	90°
Fwd. jacking case upper guide P3	0.357	0.596	0.654	0.702	135°
Aft. jacking case upper guide P4	0.344	0.573	0.631	0.695	90°
Helideck P5	0.181	0.308	0.348	0.354	135°

Under full load conditions, although the arrangement positions of tower sections, nacelles, and blades on the main deck are different, after obtaining the motion response of a certain point (such as center of gravity) of the hull, the motion response of point P at any other position of the hull can be obtained by the following method:

The displacement $\vec{r}_p$ at point P is calculated by

$$\vec{r}_p = \vec{r}_G + \mathbf{R}\vec{r}_{P/G} \tag{20}$$

$$\mathbf{R} = \mathbf{R}_x(\theta)\mathbf{R}_y(\phi)\mathbf{R}_z(\psi) = \begin{bmatrix} \cos\phi\cos\psi & -\cos\phi\sin\psi & \sin\phi \\ \cos\theta\sin\psi + \sin\theta\sin\phi\cos\psi & \cos\theta\cos\psi - \sin\theta\sin\phi\sin\psi & -\sin\theta\cos\phi \\ \sin\theta\sin\psi - \cos\theta\sin\phi\cos\psi & \sin\theta\cos\psi + \cos\theta\sin\phi\sin\psi & \cos\theta\cos\phi \end{bmatrix} \tag{21}$$

The acceleration vector $\vec{a}_P$ at point P consists of translational acceleration, tangential acceleration, and normal acceleration, and is calculated by

$$\vec{a}_P = \vec{a}_G + \dot{\vec{\omega}} \times \vec{r}_{P/G} + \vec{\omega} \times (\vec{\omega} \times \vec{r}_{P/G}) \tag{22}$$

where θ, ϕ, ψ are the roll angle (about x-axis, positive to port), pitch angle (about y-axis, positive stern down), and yaw angle (about z-axis, positive turning to port), respectively; $\vec{r}_{P/G}$ is the coordinate of point P relative to the center of gravity of the hull; $\vec{r}_G$, $\vec{a}_G$ are the displacement and acceleration responses at the center of gravity of the hull, respectively; and $\vec{\omega}$ is the angular velocity.

Through the above theoretical analysis, the variation of the WTIV motion response RAOs with spatial position can be well explained, which is mainly caused by the contribution of the tangential acceleration generated by roll/pitch to the vertical acceleration.

4.2.3. Seakeeping Evaluation and Operational Implications for WTIV

The new generation of large WTIVs integrates the functions of dynamic positioning jack-up operations and ocean-going navigation. Based on years of research on Motion Sickness Incidence (MSI) and the resulting ship motion comfort evaluation criteria, and considering the actual floating operation requirements of WTIVs, acceptable thresholds for MSI and vertical/lateral acceleration, roll, and pitch have been established for humans under different task conditions, as shown in Table 10 below [26].

Table 10. Seakeeping Evaluation Indicators for WTIV.

Description	Ocean Transit	Coastal Transit		DP and Installation
	Navy Crew	Light Manual Work	Heavy Manual Work	Demanding Work
VAcc.	0.275 g	0.2 g	0.15 g	MSI 10% *
Roll	6°	4°	4°	3°
Pitch	3°	2°	1.5°	1.5°

* 10% MSI among infrequent travelers of the general public [27]. "g" is the gravitational acceleration.

Integrating the ship comfort criteria from the table above, for WTIVs during coastal transit and DP jack-up operations—where not only the crew but also a large number of construction personnel are on board and the open deck is fully loaded with wind turbine components—the maximum significant wave height is generally controlled within 6.0 m to ensure the comfort and safety of the loaded voyage. For the DP and jack-down phase, the vessel's own DP capability and the seabed impact load on the spudcans must also be considered, leading to a more restrictive maximum significant wave height of 2.5 m.

During ocean transit conditions, where fewer wind turbine components and deck cargo are carried, the primary considerations are crew comfort and the structural strength of the legs. Under these conditions, the vessel can typically withstand a maximum significant wave height of up to 9.0 m. If more severe sea conditions are encountered, partially lowering the legs can be considered as a temporary measure to reduce the inertial loads on the leg structure induced by hull motion, thereby ensuring its structural safety.

5. Conclusions

Based on the unique hull form characteristics of the new generation of Wind Turbine Installation Vessel, this study constructed a nonlinear analysis framework of geometric mutation–vortex dissipation–damping evolution through a collaborative approach integrating model tests and CFD simulations. This framework systematically reveals the seakeeping mechanism of the WTIV. By introducing a fluid inertia coupling model for the well region, the free-flooding anti-roll tank-like effect generated by the well structure when the leg is fully retracted was clarified. Consequently, the method for evaluating the roll period and damping coefficient of high-center-of-gravity WTIVs has been refined. The main findings are as follows:

(1) The damping coefficient and natural roll period are fundamental parameters for WTIV motion analysis. This study, by fully accounting for fluid viscosity effects, quantifies for the first time the linear relationship between leg lowering depth and roll damping: the damping coefficient increases with a gradient of 0.04% per meter of lowering depth. Concurrently, as the leg is lowered and the hull's center of gravity is reduced, the natural roll period exhibits an increasing trend.

(2) In addition to fluid viscosity effects, the nonlinear characteristics of roll motion are determined by the WTIV's cross-sectional shape, spudcan volume, and well structure. Through model tests and collaborative CFD verification, this study reveals the dual-mode effect of the additional moment of inertia ($\Delta I_{XX} \approx 1.56 \times 10^7$ tm^2) from the fluid in the spudcan well area on damping characteristics. When the leg is fully retracted, damping is enhanced by approximately 58%, and the roll period is shortened by about 7%.

(3) A six-degree-of-freedom Response Amplitude Operator (RAO) frequency response model based on viscous flow theory was established. The prediction error for the extreme acceleration values at key positions is less than 10%, surpassing the accuracy limits of traditional potential flow theory. Specifically, while the potential-flow-theory-based RAO linear method is suitable for predicting motion and loads in small to moderate waves, its accuracy decreases under extreme sea states (characterized by high wave heights and large steepness) that induce large-amplitude ship motions and significant nonlinear effects (e.g., green water on deck and slamming). Under these conditions, the fully nonlinear time-domain approach considering fluid viscous effects, as presented in this study, becomes necessary for reliable simulation and analysis.

(4) The distribution pattern of the extreme motion responses of the WTIV under different wave directions was revealed: the maximum responses of roll angle and lateral acceleration occur in bow quartering seas, contrary to the beam seas suggested by traditional theory. Combined with the $max(\theta/T)$ response analysis results, a calculation method for the leg impact load during dynamic positioning (DP) operations is proposed. It is demonstrated that quartering and beam seas are the primary conditions leading to extreme vertical inertial acceleration loads, providing a critical basis for the strength design of key structures such as the leg-spudcan system, crane boom rests, and helideck.

Although grid convergence verification was performed in this study's CFD analysis, the accuracy of the results remains somewhat dependent on local mesh quality, particularly near areas with high hull surface curvature and complex appendages like spudcans and bilge keels. Furthermore, the computational domain size and simulation duration for the WTIV's motion response in irregular waves were constrained by available computing resources and cost. To address these limitations, future work should focus on developing more efficient and accurate simulation strategies suitable for large-scale practical engineering applications. This includes research on wave–structure–seabed coupled dynamics to move beyond the current rigid seabed assumption and achieve multi-physical field coupling analysis. Additionally, based on the discovered "free-flooding anti-roll tank"-like effect in the leg-spudcan well region, further research into anti-rolling technology adapted to high sea states in deep-sea environments is warranted. Optimizing parameters such as well volume and outflow rate could help achieve optimal anti-rolling performance across various sea conditions.

Author Contributions: M.X.: conceptualization, data curation, formal analysis, investigation, methodology, validation, writing—original draft, writing—review and editing. Y.W.: project administration, supervision, writing—review and editing. J.W.: data curation, formal analysis, methodology, X.L.: data curation, validation and editing. W.L.: data curation, methodology, writing—review and editing. D.Y.: data curation, methodology, validation, writing—review and editing, resources. All authors have read and agreed to the published version of the manuscript.

Funding: This research received no external funding.

Institutional Review Board Statement: Not applicable.

Informed Consent Statement: Not applicable.

Data Availability Statement: The data presented in this study are available upon request from the corresponding author.

Acknowledgments: This research was supported by the design of series WTIV project funded by Marine Design & Research Institute of China. The authors would like to gratefully acknowledge Offshore Engineering Department for supplying the information and data, Kang Weixia for providing the detail information of the series WTIV and Wu Yongshun for their participation in the installation, conduction, and evaluation of the seakeeping experiment.

Conflicts of Interest: The authors declare that they have no known competing financial interests or personal relationships that could have appeared to influence the work reported in this paper.

References

1. Xiahou, M.; Yang, D.; Liu, H.; Shi, Y. Investigation on Calm Water Resistance of Wind Turbine Installation Vessels with a Type of T-BOW. *J. Mar. Sci. Eng.* **2024**, *12*, 1337. [CrossRef]
2. Guo, Y.; Wang, H.; Lian, J. Review of integrated installation technologies for offshore wind turbines: Current progress and future development trends. *Energy Convers. Manag.* **2022**, *255*, 115319. [CrossRef]
3. Det Norske Veritas (DNV). *DNV-RP-C104 Self-Elevating Units*; DNV: Veritasveien, Norway, 2015.
4. Lucintel. *Report on the Current Situation and Future Prospects of China's Offshore Wind Turbine Installation Vessel Industry (2024–2031)*; Lucintel: Irving, TX, USA, 2025.
5. Xu, C.; Sun, L.P.; Zhao, Z.J.; Zhang, L.J. Motion Response Analysis and Model Test Research of Wind Turbine Installation Vessel. *Ship Stand. Eng.* **2016**, *49*, 37–42. [CrossRef]
6. Xu, C. Research on Hull Line Optimization and Hydrodynamic Performance of Wind Turbine Installation Vessel. Master's Thesis, Harbin Engineering University, Harbin, China, 2016.
7. Zhang, W.; Liu, Y.D.; Zheng, G.Y.; Chen, C.; Tang, Y.Y. Parametric Roll Analysis of KCS Container Ship Based on Potential Flow Theory. *Ship Eng.* **2022**, *44*, 426–434.
8. Jiao, J.L.; Huang, S.X.; Chen, C.H. Seakeeping Prediction of Ship in Short Crested Waves Based on RANS. *Shipbuild. China* **2020**, *61*, 152–157.

9. Guo, J.; Sun, S.Z.; Ren, H.L. Experimental Study on Seakeeping Performance of Large-Scale Ship Model in Coastal Wind Waves. *Ship Sci. Technol.* **2015**, *37*, 59–64.
10. Song, Z.F.; Chen, C.H. Hydrodynamic Performance Analysis of Offshore Wind Farm Operation and Maintenance Mother Ship Based on STAR-CCM+. *Guangdong Shipbuild.* **2024**, *43*, 17–21.
11. Song, X.; Jia, L.; Chen, C. CFD Prediction of Ship Seakeeping Behavior in Bi-Directional Cross Wave Compared with in Uni-Directional Regular Wave. *Appl. Ocean Res.* **2020**, *104*, 102426.
12. Li, T.L.; Huang, Z.Q.; Tong, M.Y. Optimization Design of Bilge Keel for Ocean Squid Fishing Vessel Based on CFD Method. *Chin. J. Ship Res.* **2024**, *19*, 27–34.
13. Feng, J. Research on Drag Reduction Optimization and Seakeeping Performance of Offshore Wind Catamaran Service Operation Vessel Based on CFD. Master's Thesis, Dalian Ocean University, Dalian, China, 2023.
14. Irkal, M.A.; Nallayarasu, S.; Bhattacharyya, S. CFD Approach to Roll Damping of Ship with Bilge Keel with Experimental Validation. *Appl. Ocean Res.* **2016**, *55*, 1–17. [CrossRef]
15. Kianejad, S.; Lee, J.; Liu, Y.; Enshaei, H. Numerical Assessment of Roll Motion Characteristics and Damping Coefficient of a Ship. *J. Mar. Sci. Eng.* **2018**, *6*, 101. [CrossRef]
16. Devolder, B.; Stempinski, F.; Mol, A.; Rauwoens, P. Roll Damping Simulations of an Offshore Heavy Lift DP3 Installation Vessel Using the CFD Toolbox OpenFOAM. In Proceedings of the International Conference on Offshore Mechanics and Arctic Engineering, Houston, TX, USA, 1–5 June 2020; p. V008T08A045.
17. Ghamari, I.; Mahmoudi, H.R.; Hajivand, A.; Seif, M.S. Ship Roll Analysis Using CFD-Derived Roll Damping: Numerical and Experimental Study. *J. Mar. Sci. Appl.* **2022**, *21*, 67–79. [CrossRef]
18. Kjær, R.B.; Shao, Y.; Walther, J.H. Experimental and CFD Analysis of Roll Damping of a Wind Turbine Installation Vessel. *Appl. Ocean Res.* **2024**, *143*, 103857. [CrossRef]
19. Gao, J.; He, Z.; Zang, J.; Chen, Q.; Ding, H.; Wang, G. Topographic Effects on Wave Resonance in the Narrow Gap between Fixed Box and Vertical Wall. *Ocean Eng.* **2019**, *180*, 97–107. [CrossRef]
20. Ding, Y.; Walther, J.H.; Shao, Y. Higher-Order Gap Resonance between Two Identical Fixed Barges: A Study on the Effect of Water Depth. Phys. *Fluids* **2022**, *34*, 052113. [CrossRef]
21. Lei, W.; Chen, J.; Shao, Y.; Yu, X. CFD-Assisted Linearized Frequency-Domain Analysis of Motion and Structural Loads for Floating Structures with Damping Plates. *Ocean Eng.* **2023**, *281*, 114924. [CrossRef]
22. Sheng, Z.B.; Liu, Y.Z. *Ship Theory (Volume 2)*; Shanghai Jiao Tong University Press: Shanghai, China, 2008; pp. 154–196.
23. Xie, Y.L. Research on Slamming Load Characteristics of the Seventh Generation Ultra-Deepwater Drilling Platform. Master's Thesis, Jiangsu University of Science and Technology, Zhenjiang, China, 2019.
24. Siemens. *Simcenter STAR-CCM+ User Guide, 2022.1*; Software User Manual, Siemens Digital Industries Software: Plano, TX, USA, 2022.
25. Lin, Y.; He, J.Y. Ship Resistance and Free Motion Prediction Based on RANS Method. *Ship Eng.* **2019**, *41*, 52–57.
26. Xiahou, M.; Yang, D.; Kang, W.; Chi, J.; Cheng, W. Method for the Operational Weather Window Assessment of Self-Elevating Wind Turbine Installation Vessels. In Proceedings of the 2024 International Conference on Intelligent Ships and Electromechanical System, Guangzhou, China, 27–29 December 2024; p. 156.
27. O'Hanlon, J.F.; McCauley, M.E. Motion sickness incidence as function of the frequency and acceleration of vertical sinusoidal motion. *Aerosp. Med.* **1974**, *45*, 366–369. [PubMed]

Disclaimer/Publisher's Note: The statements, opinions and data contained in all publications are solely those of the individual author(s) and contributor(s) and not of MDPI and/or the editor(s). MDPI and/or the editor(s) disclaim responsibility for any injury to people or property resulting from any ideas, methods, instructions or products referred to in the content.